Physica D 333 (2016) 254–265

Contents lists available at ScienceDirect

Physica D

journal homepage: www.elsevier.com/locate/physd

Traveling waves for a model of gravity-driven film flows in cylindrical domains

Roberto Camassa [a], Jeremy L. Marzuola [a], H. Reed Ogrosky [b,*], Nathan Vaughn [a]

[a] Department of Mathematics, University of North Carolina-Chapel Hill, Phillips Hall, Chapel Hill, NC 27599, USA

[b] Department of Mathematics, University of Wisconsin-Madison, Van Vleck Hall, Madison, WI 27599, USA

HIGHLIGHTS

- Study a fully nonlinear dissipative/dispersive wave propagation model.
- Explore mean thickness threshold for traveling wave formation for viscous films.
- Compare threshold results to experiments.

ARTICLE INFO

Article history:
Received 2 September 2015
Received in revised form
9 December 2015
Accepted 12 December 2015
Available online 19 December 2015

Keywords:
Thin films
Traveling waves
Numerical continuation

ABSTRACT

Traveling wave solutions are studied for a recently-derived model of a falling viscous film on the interior of a vertical rigid tube. By identifying a Hopf bifurcation and using numerical continuation software, families of non-trivial traveling wave solutions may be traced out in parameter space. These families all contain a single solution at a 'turnaround point' with larger film thickness than all others in the family. In an earlier paper, it was conjectured that this turnaround point may represent a critical thickness separating two distinct flow regimes observed in physical experiments as well as two distinct types of behavior in transient solutions to the model. Here, these hypotheses are verified over a range of parameter values using a combination of numerical and analytical techniques. The linear stability of these solutions is also discussed; both large- and small-amplitude solutions are shown to be unstable, though the instability mechanisms are different for each wave type. Specifically, for small-amplitude waves, the region of relatively flat film away from the localized wave crest is subject to the same instability that makes the trivial flat-film solution unstable; for large-amplitude waves, this mechanism is present but dwarfed by a much stronger tendency to relax to a regime close to that followed by small-amplitude waves.

1. Introduction

The flow of falling liquid films is a topic of importance in several disciplines including biology and engineering. These films have a free surface whose evolution is governed by the interplay of body forces (gravity) and surface stresses (due to the surface tension of the free surface). Numerous modeling and experimental studies have advanced understanding of these flows in a variety of regimes corresponding to different parameter values (e.g., Reynolds number, Bond number, etc.), and in a number of geometrical setups including (i) along an inclined plane (e.g., [1,2]) and (ii) the exterior or interior of a vertical tube (e.g., [3–7]); see also [8]. The cylindrical geometry of the tube is distinct from the planar case due to the role of the free surface's azimuthal curvature in setting the surface stresses. This geometry is the focus of the current study, where we further concentrate on the cylinder *interior* problem. In contrast with its exterior film counterpart, this setup poses a natural limit to the thickness of the film, corresponding to cases when the surface tension azimuthal component drives the free surface all the way to the cylinder axis. When this happens, plugs of fluid that can fill sections of the tube are formed, up to the limit when the entire tube is filled with liquid moving according to the Poiseuille flow solution of the motion equations.

More specifically, the problem studied here is the gravity-driven downward flow of a highly viscous liquid film that coats the interior of a vertical rigid tube. While highly idealized, this particular setup is of interest due to its potential relevance for understanding the flow of the thin layer of mucus which lines

* Corresponding author.
E-mail addresses: camassa@amath.unc.edu (R. Camassa), marzuola@math.unc.edu (J.L. Marzuola), ogrosky@math.wisc.edu (H.R. Ogrosky), njvaughn@umich.edu (N. Vaughn).

http://dx.doi.org/10.1016/j.physd.2015.12.003
0167-2789/

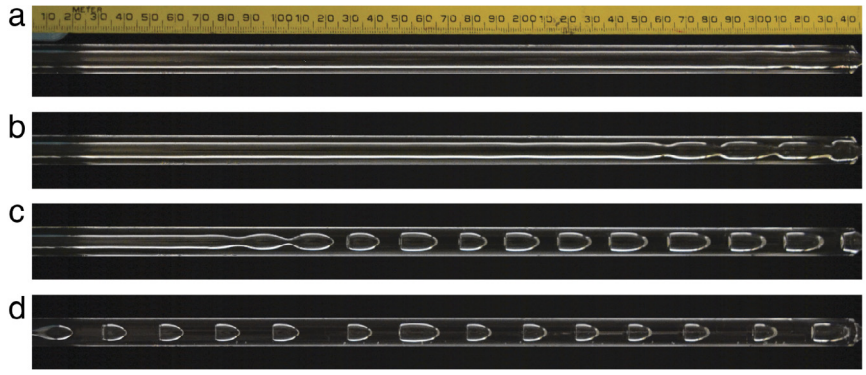

Fig. 1. Snapshots of four experiments with $\rho = 0.97$ g cm^{-3}, $\mu = 129$ P, $\gamma = 21.5$ dyn cm^{-1}, and $a = 0.5$ cm. The film thickness of each panel was measured to be (a) $h_0 = 0.223$ cm, (b) $h_0 = 0.256$ cm, (c) $h_0 = 0.295$ cm, and (d) $h_0 = 0.331$ cm. (Each snapshot is rotated by 90° with respect to the actual experiment, so that acceleration due to gravity acts from left to right.)
Source: Reproduced from [7].

human airways. The problem was studied experimentally in [7], where a fixed volume flux of a high-viscosity silicone oil was fed through an axisymmetric slit into the interior of a 40 cm long vertical tube. Once the entire tube was coated with oil, the free surface of the oil film was observed as it fell down the tube wall.

In these experiments, two distinct flow regimes were observed, distinguished from one another by a critical film thickness (as a function of other flow parameters). For relatively thick films, the free surface was observed to be unstable, with disturbances growing as they traveled down the tube until they 'pinched off' and formed liquid plugs clogging the tube; these plugs continued to travel downwards, eventually exiting the bottom of the tube. For thin films, the free surface either did not exhibit any observable instability growth or showed instabilities that remained small and did not clog the tube. In all observations, the film flow was observed to be axisymmetric; see Fig. 1.

Strongly nonlinear models for the axisymmetric flow studied here have typically been derived by assuming a small ratio of lengthscales and fall into one of two categories. Thin-film models rely on a small film thickness compared with the tube radius [3,9], while long-wave models utilize a small film thickness relative to a typical wavelength of free-surface disturbances [4,7]. See [10] for further discussion of this classification.

We next summarize a single-PDE long-wave model recently derived in [7]. The derivation of the model relies on both the aforementioned small long-wave aspect ratio and an assumed small Reynolds number so that inertia may be neglected. The dimensional form of the model is

$$\mu R_t = \rho g f_1(R; a) R_z + \frac{\gamma}{16R}[f_2(R; a)(R_z + R^2 R_{zzz})]_z, \tag{1}$$

where z is the independent axial coordinate and $R(z, t)$ denotes the position of the free surface. Here z is oriented so that gravity acts in the positive z direction; $r = 0$ denotes the center of the tube and $r = a$ denotes the tube wall. Experimental parameters include the fluid's molecular viscosity μ, density ρ, and surface tension γ; g is acceleration due to gravity. Subscripts will be used throughout the paper to denote partial derivatives, and the functions f_i are given by

$$f_1(R; a) = \frac{1}{2}[R^2 - a^2 - 2R^2 \log(R/a)], \tag{2a}$$

$$f_2(R; a) = -\frac{a^4}{R^2} + 4a^2 - 3R^2 + 4R^2 \log(R/a). \tag{2b}$$

The first term on the right-hand side (RHS) of (1) represents the effects of gravity; the remaining two terms represent the effects of surface tension acting through the azimuthal and axial curvatures of the free surface, respectively. The model (1) may also be expressed as a conservation law for the quantity R^2,

$$8\mu(R^2)_t = \{f_2(R; a)[-\rho g R^2 + \gamma(R_z + R^2 R_{zzz})]\}_z, \tag{3}$$

so that the model conserves the volume $\pi(a^2 - R^2)$ of the fluid film. This conservation of volume is one of the features distinguishing 'long-wave' models from most 'thin-film' models, which usually conserve an approximate volume $2\pi a(a - R)$ in this cylindrical geometry. For reference, the model equation is given in dimensionless form as well in the Appendix, however in what follows we will use the full dimensional form of the model equations for the most part.

For each mean film thickness $h_0 = a - R_0$, there is a trivial solution $R(z, t) = R_0$ to (1). This constant free surface is unstable to long-wave disturbances, consistent with linear stability results for the governing equations in this and related setups [11–13]; specifically, if a disturbance of the form $R = R_0 + A \exp[\mathrm{i}(kz - \omega t)]$ is introduced to the model equation (1), the resulting dispersion relation is

$$\omega = -\frac{\rho g}{\mu} f_1(R_0; a)k + \frac{\mathrm{i}\gamma}{16\mu R_0}\left[f_2(R_0; a)(-k^2 + R_0^2 k^4)\right]. \tag{4}$$

Thus the flat solution is unstable to a band of small wavenumbers $0 < k < R_0^{-1}$, with the fastest-growing wavenumber given by

$$k_m = (\sqrt{2}R_0)^{-1}. \tag{5}$$

The dispersion relation (4) has the same form as that of the well-studied Kuramoto–Sivashinsky (K–S) equation, first shown to be a limiting form of a model for film flow down an inclined plane [1,2] by Sivashinsky and Michelson [14].

When the model (1) is solved numerically using periodic boundary conditions and initial conditions consisting of a flat free surface perturbed by a superposition of several small-amplitude Fourier modes, the initial growth of the disturbances is well described by (4). As the perturbations grow beyond the weakly nonlinear regime, solutions exhibit one of two distinct types of behavior. For relatively thin films, the disturbances saturate as a series of traveling pulses which undergo various nonlinear interactions with one another, but generally hold their shape and propagate approximately as a coherent wave train. For thicker films, however, the fastest-growing disturbance continues to grow, apparently accelerated rather than saturated by nonlinearities in the model. This wave crest grows until its amplitude approaches the tube radius $r = 0$, with the latter stages of this growth occurring very rapidly. Due to the cylindrical geometry present in the model, as seen in the inverse powers and logarithms of R in (1), solutions cannot be computed once this crest reaches the tube

center $r = 0$ (and the assumptions on which the model is based break down as well), but the instability appears to grow arbitrarily close to the center in finite time. These solutions thus suggest that, for these thicker films, the film tends towards 'choking' or 'clogging' the tube.

Traveling wave (TW) solutions to the model (1) were also found in [7] for the representative case of tube radius $a = 0.5$ cm by 'clipping' a single pulse from a snapshot of the free surface's evolution sufficiently long after the saturation of instabilities and feeding this wave profile into a boundary value-problem (BVP) solver. For thicker films whose free-surface instabilities do not saturate but exhibit unchecked growth, this method obviously could not be used, but a search for traveling wave solutions for these thicker films was made by continuation of the thinner-film TW solutions in parameters like mean film thickness. While many traveling wave solutions were found using this approach, a critical film thickness was found to exist; for films thicker than this critical thickness, no TW solutions were found. A critical film thickness separating two flow regimes was thus identified for the problem from three distinct perspectives: (i) the presence or absence of plug formation in experiments, (ii) the existence or non-existence of apparent finite-time singularities in the model (1), and (iii) the existence or non-existence of traveling wave solutions to the model, respectively.

In [7] it was found that these critical thicknesses were all in good agreement with one another for a representative tube radius $a = 0.5$ cm; in addition, the critical thicknesses as determined by the physical experiments and transient solutions to (1) were in good agreement for a variety of tube radii. In this work, we explore the branching of traveling wave profiles and existence of critical turnaround points as the mean thickness varies by observing the traveling waves arise out of a natural Hopf bifurcation for the flat solution that can be computed analytically. As a result of this Hopf bifurcation, families of traveling waves can be easily computed for any tube radius and the critical mean thickness beyond which the branches cease to exist numerically approximated via continuation methods. Once again, remarkably these turnaround points are in very good agreement with the plug formation observed experimentally in [7]. This agreement is remarkable for several reasons. For one, several approximations were made in deriving the model equation, yet the level of quantitative agreement with the physical experiments was quite good. In particular, it is somewhat surprising that an asymptotic model which depends on a small aspect ratio of length scales would be able to accurately predict plug formation. For another, periodic boundary conditions were used to solve the model while the boundary conditions of the experiment were certainly not periodic. What is more, the traveling wave solutions used to estimate the critical values of the parameters distinguishing one regime from another were of a fixed period (and a different period than that observed in the experiments) despite the search for solutions over a wide range of parameter values.

Other models of low-Reynolds number film flows in different geometries have been shown to have similar finite-time singularities, though the physical interpretation of this behavior is dependent on the problem setup. For example, finite-time singularities in a thin-film model derived in [1,2] for flows down an inclined plane are interpreted as indicative of film break-up [15]. The fact that such break-up is not observed in experiments has partly motivated the development of new modeling approaches such as integral boundary layer models in, e.g., [16], that consist of coupled systems of PDEs. These alternate models do not exhibit finite-time singularities, providing improved agreement with experiments. Finite-time singularities in a thin-film model for flows down the exterior of a tube [3,17] have been interpreted as indicating drop formation [18]. This behavior is not limited to thin-film models; other one-equation models including an exterior-flow long-wave model that is analogous to the interior-flow model considered here also exhibit blowup.

In contrast, in the present setup this model behavior appears to be a good indicator of plug formation in the tube. We note that the possibility of plug formation provides an important distinction between interior and exterior flows. At the moment plug formation occurs in interior flows, the change in the free surface topology may be expected to render asymptotic models helpless to describe any subsequent changes in the film flow. Finite-time singularities in such models may therefore be considered less of a model shortcoming and more as an additional source of information about the timing and route to plug formation.

Exploring the mathematical and physical connections between these three perspectives, i.e. transient solutions to the model, traveling wave solutions, and physical experiments, is the primary topic of the current work. We will first discuss in Section 2 the computational aspects of finding traveling solutions for Eq. (1), including locating the critical Hopf bifurcation from the flat solution, which offers an alternative viewpoint to the task of finding traveling wave solutions as saturation of the flat solution stability analysis expressed by the dispersion relation (4). In Section 3, the correspondence between the turnaround point of solution branches and the formation of plugs in physical experiments is studied for a variety of parameter values. The stability of the solutions will be discussed in Section 4. Conclusions and topics for further work will be discussed in Section 5.

2. Traveling wave solutions

Traveling wave solutions may be found by substituting $R(z,t) = Q(z-ct)$ into the model equation (1) to obtain a fourth order ODE in z,

$$\rho g f_1(Q;a)QQ_z + \frac{\gamma}{16}[f_2(Q;a)(Q_z + Q^2Q_{zzz})]_z + c\mu QQ_z = 0, \quad (6)$$

where c is the speed of the wave. Since this is a perfect derivative however, we can integrate once to obtain

$$\rho g f_3(Q;a) + \frac{\gamma}{16}[f_2(Q;a)(Q_z + Q^2Q_{zzz})] + \frac{c\mu}{2}Q^2 = K, \quad (7)$$

where

$$f_3(Q;a) = -\frac{1}{2}a^2Q^2 + \frac{3}{8}Q^4 - \frac{1}{2}Q^4\log\frac{Q}{a},$$

and the constant of integration K becomes another parameter we can vary in our simulations.

2.1. Hopf bifurcations

Eq. (7) can be solved exactly for flat solutions, using for instance the '*fsolve*' command in *Matlab* (or by searching for equilibrium solutions in numerical continuation software such as *AUTO* or *Matcont*). This gives a family of flat states that can then be studied from the point of view of stability. Unless otherwise stated, the experimental parameter values $\rho = 0.97$ g cm^{-3}, $\mu = 129$ P, $\gamma = 21.5$ dyn cm^{-1} used in [7] will also be used here.

Locating the Hopf bifurcation involves three parameters: speed c, integration constant K, and the flat solution Q. While there is an infinite set of these parameter values that solve the equation for the flat case, we would like a good starting point in order to find the Hopf point that will evolve into non-trivial traveling wave solutions. First we find a reasonable value for K by running the pseudospectral evolution code. Starting with a quasi-randomly perturbed flat state, we ran the pseudospectral code for a long enough time for it to reach its saturated regime of wave trains. Determining the wave speed, Q, Q_z, and Q_{zz} from this data allows us

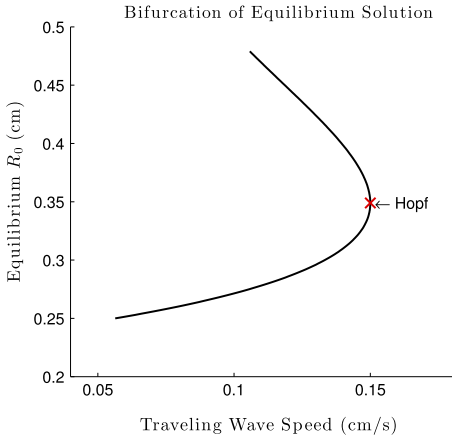

Fig. 2. Equilibrium solution $Q = R_0$ versus wave speed for $a = 0.5$ cm, with $K = 0.2146$ as determined by the pseudospectral code.

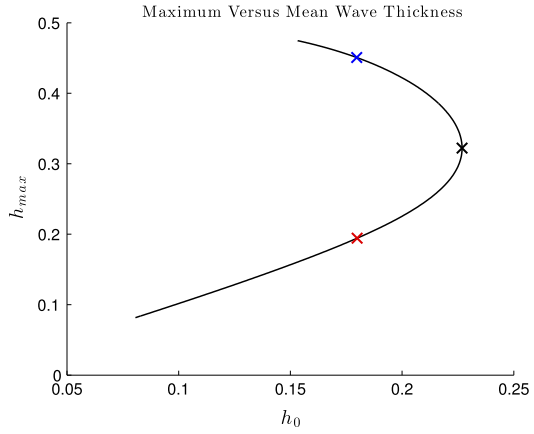

Fig. 3. Branches of traveling wave solutions showing the maximum film thickness $h_{\max}$ versus the mean film thickness $h_0 = a - Q_0$ for wave with period $L = 2\pi$ in a tube radius of $a = 0.5$ cm. Red and blue '×'s indicate representative waves from the lower and upper branch, respectively; these waves are shown in Fig. 4. Black '×' indicates the turnaround point h_c. (For interpretation of the references to color in this figure legend, the reader is referred to the web version of this article.)

to calculate the corresponding integration constant, K, to use when we integrate the 4th order ODE (6). This K value corresponds to the low amplitude wave trains, not to the flat solution, but it is in the neighborhood of its corresponding bifurcation value. The fact that this K value is attained by the time evolution code assures that a bifurcation search stems from a physical or achievable regime for the fluid.

Having determined a starting value for K, we are in position to determine the corresponding equilibrium flat solutions Q_f. As z-derivatives of Q_f are zero Eq. (6) reduces to

$$\rho g f_3(Q_f; a) + c\frac{\mu}{2}Q_f^2 = K, \tag{8}$$

which then fixes the relationship between the remaining parameters Q_f and c.

Next, linearizing the 3rd order ODE (7) in terms of these parameters generates the Jacobian matrix,

$$J = \begin{bmatrix} 0 & 1 & 0 \\ 0 & 0 & 1 \\ J_1(Q_f) & -Q_f^{-2} & 0 \end{bmatrix}, \tag{9}$$

where

$$J_1(Q) = \frac{16K}{\gamma}\frac{d}{dQ}\left[\frac{1}{f_2 Q}\right] - \frac{8c\mu}{\gamma}\frac{d}{dQ}\left[\frac{1}{f_2}\right] - \frac{16\rho g}{\gamma}\frac{d}{dQ}\left[\frac{f_3}{f_2 Q^2}\right] + \frac{2Q_z}{Q^3}. \tag{10}$$

For a fixed value of K, we sweep through a range of values for Q_f (and hence c, see Fig. 2), evaluating the Jacobian and computing its eigenvalues at each step. The Jacobian J has one real eigenvalue and a pair of complex conjugate eigenvalues. The Hopf bifurcation is determined by the complex pair crossing from negative real components to positive real components with nonzero speed as the parameters are varied; see Fig. 2 for $K = 0.2146$. The same conclusion about the location of the Hopf point can be obtained by the alternative method of finding the phase speed $c = \omega(k)/k$ corresponding to the film thickness such that the first Fourier modes $k = \pm(R_0)^{-1}$ coincide with edge of the flat solution instability window from (4). From this Hopf bifurcation point, the *AUTO* software package (see [19]) is used to continue off of the equilibrium branch and onto non-trivial traveling waves.

2.2. Traveling waves

The Hopf bifurcation off of flat solutions found by *AUTO* for the full ODE system has a zero eigenvalue occurring simultaneously with the complex pair crossing the imaginary axis. This so-called zero-Hopf bifurcation point makes the numerical continuation of the associated solution branch more complicated, and it becomes convenient for this purpose to use a slightly smoothed equation

$$-\epsilon Q_{zz} + \rho g f_3(Q; a) + \frac{\gamma}{16}[f_2(Q; a)(Q_z + Q^2 Q_{zzz})] + \frac{c\mu}{2}Q^2 = K, \tag{11}$$

where the additional viscosity term with weight ϵ makes the bifurcation a pure Hopf bifurcation. A similar approach is taken in the recent work [20], as well as discussed in [21]. Following the (identical) family of flat solutions for (11) isolates a pure Hopf bifurcation that gives rise to a family of periodic orbits. Once we are on the periodic branch, we can continue with the limit $\epsilon \to 0$ and truly work with numerical solutions to (7). Numerically, we first continue in c and the period to find solutions of period $L = 2\pi$. This primarily serves the purpose of comparison with waves observed in [7], but also allows to fix a reference tube length with which one can then study variations of other parameters such as the tube radius.

Continuing off this period 2π solution in c and the integration constant K, we observe a family of traveling waves that has a critical 'turnaround' point in the mean thickness, h_c; such a branch and turnaround point are shown in Fig. 3 where $h_c \approx 0.225$ cm, and the corresponding maximum thickness of the film at this turnaround point is $h_{\max_c} \approx 0.32$ cm. This family of solutions thus contains multiple traveling wave solutions for some mean thicknesses $h_0 < h_c$ (with all other flow parameters fixed), while the family of solutions contains no solutions for $h_0 > h_c$. Samples of two wave profiles from Fig. 3 are given in Fig. 4; one 'upper branch' or large-amplitude wave with $h_{\max} > h_{\max_c}$, and one 'lower branch' or small-amplitude wave with $h_{\max} < h_{\max_c}$.

AUTO allows further continuation of the periodic solutions in the tube radius a. As a result a large family of turnaround points can be computed simply by continuing nearby curves. However, the search is complicated by what appears to be a fold bifurcation at low tube radii (<0.2 cm), requiring the numerical continuation to be carried out by recomputing the Hopf bifurcations at that radius and continuing as before.

As an interesting byproduct of the numerical continuation method, we can locate via further critical bifurcations another family of traveling waves that have a double hump structure. After finding the Hopf bifurcation for a smaller radius, $a = 0.17$ cm,

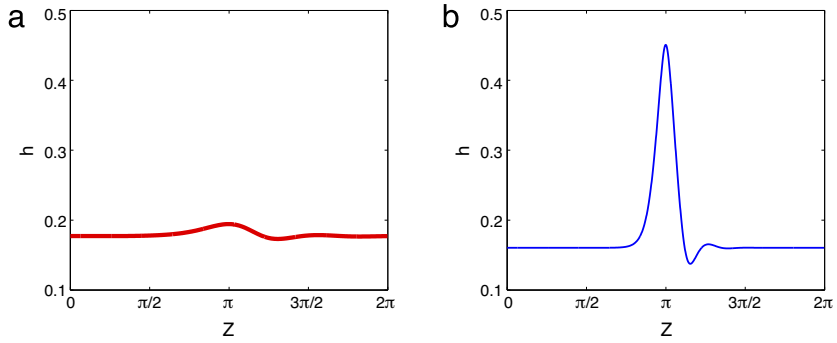

Fig. 4. Traveling wave solutions corresponding to the (a) lower branch solution (red '×') and (b) upper branch solution (blue '×') in Fig. 3 plotted as $h = a - Q$ for $a = 0.5$ cm and $h_0 = 0.18$ cm. (For interpretation of the references to color in this figure legend, the reader is referred to the web version of this article.)

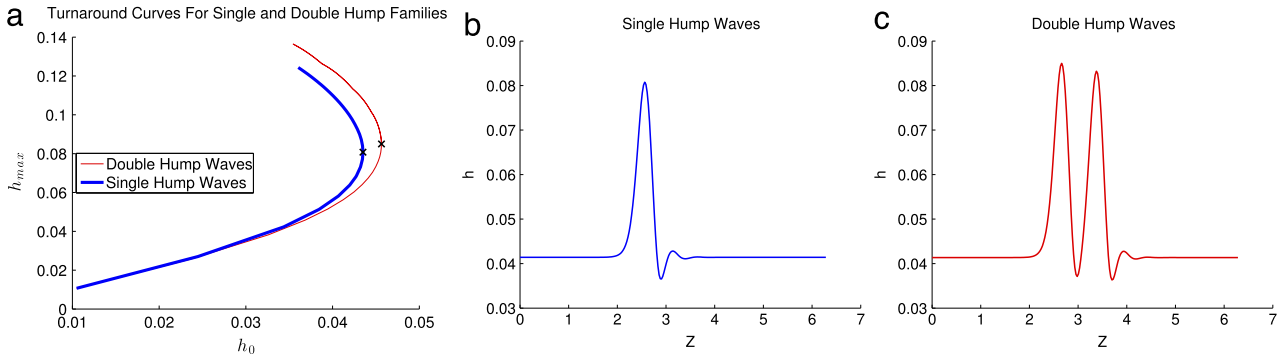

Fig. 5. (a) Families of single and double hump traveling wave solutions for $a = 0.17$ cm and $L = 2\pi$ cm. The further right curve (red) corresponds to the family of double hump waves, while the left curve (blue) corresponds to single hump waves. The ×'s mark the turnaround points. (b) A wave from the single hump family, taken from the turnaround point where $h_0 = 0.0435$ cm and $h_{\max} = 0.08075$ cm. (c) A wave from the double hump family, taken from the turnaround point where $h_0 = 0.0456$ cm and $h_{\max} = 0.08500$ cm. (For interpretation of the references to color in this figure legend, the reader is referred to the web version of this article.)

the corresponding turnaround curve for $h_{\max}$ as a function of h_0 can be computed with the same technique as for the radius $a = 0.5$ cm. A new bifurcation point can be detected low on the turnaround curve, where $h_0 = 0.01067$ cm and $h_{\max} = 0.01048$ cm, with nearly flat wave. Following the periodic solution branch downwards towards the perfectly flat solution, the branch turns back on itself and traces a new turnaround curve upwards. The waves on this new turnaround curve have two humps instead of one; see Fig. 5. The family of double hump waves attains a slightly larger critical $h_{\max}$, 0.0456 cm as opposed to the single hump family's 0.0435 cm. This seems to indicate that the location of turnaround point depends, besides the period, on the nature of the traveling wave solution being sought, i.e., whether we are looking at single hump, two humps, multiple humps, etc. However, in all cases we have examined, we found that this dependence is weak, especially in the larger tube radii, $a > 0.21$ cm. For instance, in the case above, although there are now two pulses within the 2π domain – which is similar in nature to having consecutive π periodic single hump waves – the turnaround point differs by less than 5% with respect to the single hump wave for the same period. While multiple hump solutions are interesting, in many applications they are generically less stable than their single hump counterparts, hence we will focus primarily on analysis of the single hump solutions in the current work. Similar multiple pulse branches have also been observed in other fluids models recently, see for instance [22,23].

The two hump solution turnaround points begin to differ more significantly in thinner tubes. We conjecture however that there is an upper bound of all these different turnaround points for a given period, though we have not followed more than the two hump solution branch numerically. If this is correct, the physical significance of the turnaround points we have computed must possibly be modified to imply that plug formation occurs for mean thicknesses larger than this supposedly existing upper bound for turnaround points at a fixed period. It is likewise interesting to conjecture that such an upper bound exists for all tube radii; while turnaround points were identified for all tube radii considered here, we leave further study of this question to future work.

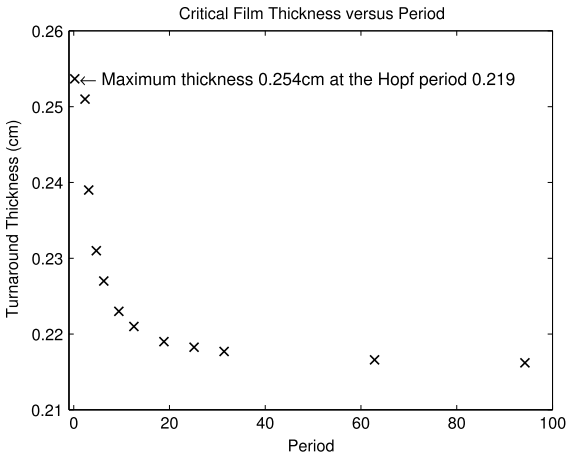

Fig. 6. Critical thickness h_c associated with the turnaround point for $a = 0.5$ cm for twelve periods ranging from the Hopf period of 0.219 cm up to 30π cm. This critical thickness is weakly dependent on period, especially for large periods (beyond $L \cong 8\pi$ cm).

The sensitivity of the critical turnaround point to the period length of single-hump traveling wave solutions is summarized in Fig. 6 for $a = 0.5$ cm. While the turnaround point is a function of period length, the value of h_c from the Hopf period to a period of 100 cm varies by only 8% of the tube radius a. The

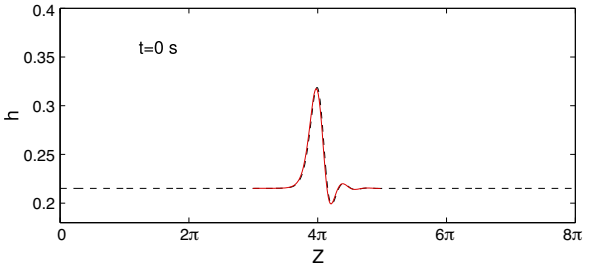

Fig. 7. Traveling wave solutions for $a = 0.5$ cm with critical thickness h_c for period $L = 2\pi$ (solid red line) and $L = 8\pi$ (dashed black line). (For interpretation of the references to color in this figure legend, the reader is referred to the web version of this article.)

remarkable agreement between the turnaround points, calculated here for a variety of periods and tube radii, and the existence of plugs strengthens the argument that these turnaround points can be used to predict the long-time behavior of these films in experiments. The profile for traveling wave solutions at the critical thickness h_c is shown in Fig. 7 for two different periods. The waves' amplitude, base of support, and the thickness away from the crest are very similar, suggesting that the decrease in critical thickness as the period length increases appears to be due to the wave's base of support remaining fixed while the flat region away from the crest widens. The thickness away from the crest thus appears to be the limiting value of turnaround thickness in Fig. 6 for large period length.

Before turning to this physical interpretation, we close this section with a comment about the limit $L \to \infty$, which would of course yield solitary wave solutions as the limit of periodic traveling waves. As Fig. 6 shows, periodic solutions and their turnaround point merging upper and lower branches can be continued by *AUTO* to large periods, $L \cong 100$ cm. This suggests that solitary traveling wave solutions could exist for model (1), though we do not pursue this issue here and leave this particular point to be more fully investigated in the future.

3. Turnaround points: physical interpretation

We next consider the physical interpretation of the critical turnaround points computed in the previous section. As discussed in the introduction, two basic types of behavior were seen in the physical experiments conducted in [7], namely the presence or absence of plugs in the tube. Fig. 1(b)–(d) shows snapshots of thick films exhibiting plug formation with $a = 0.5$ cm; panel (a) shows a snapshot of a thinner film that displays some instability growth, but the instabilities do not form plugs prior to exiting the tube. Numerical solutions to the evolution equation (1) also showed two types of behavior, namely the presence or absence of a tendency to form singularities in finite times. An example of each type of behavior can be seen in Figs. 8–9.

Fig. 8 shows a solution in which the free surface settles into a series of traveling pulses which, though interacting with one another, keep roughly constant amplitude and shape. These interactions are similar to those revealed in numerical studies of other models for thin films, and systematic coherent-structure theories have been developed to describe these interactions for several models of Newtonian films flowing down planes, including a thin-film model derived in [1], a generalized K–S equation, and a two-equation model derived in [16]; see, e.g., [24–29]. Likewise, a discussion of pulse interaction in film flows down the exterior of a tube is given in [30] for a two-equation model developed in [31], and we note that it would be interesting to see such theories developed for film flows down the interior of a tube considered here. On the other hand, Fig. 9 shows a solution in

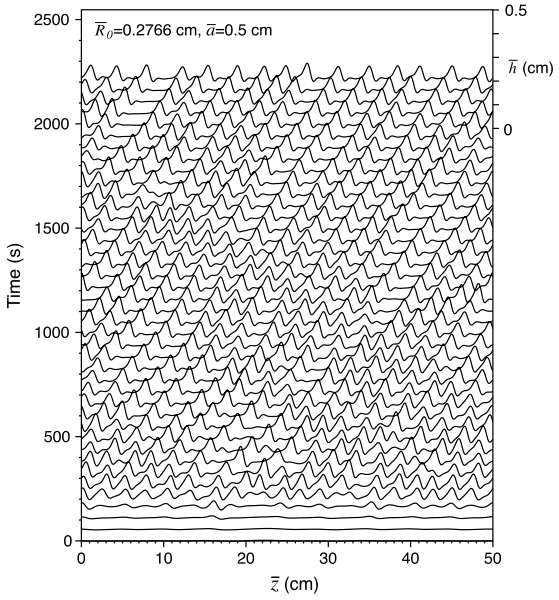

Fig. 8. Time snapshots showing the evolution of solutions to Eq. (1) in a periodic domain. Interfacial profiles $h(z, t)$ are shown successively shifted at time intervals Δt. Profiles are shown in the frame of reference moving with an undisturbed interface. The scale for h is given on the right axis for the final profile shown. Acceleration due to gravity acts from left to right; $a = 0.5$ cm, $R_0 = 0.2766$ cm and $\Delta t \approx 55$ s.
Source: Reproduced from [7].

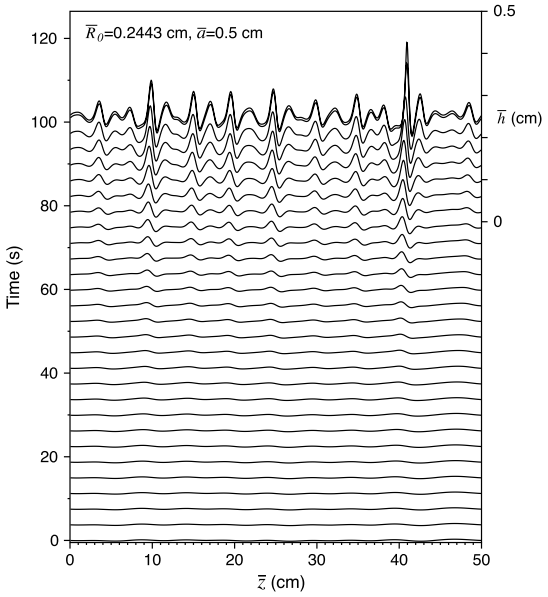

Fig. 9. Same as Fig. 8 but with $R_0 = 0.2443$ cm, $\Delta t \approx 3.75$ s. (For the final profile, $\Delta t \approx 0.56$ s.)
Source: Reproduced from [7].

which the free surface becomes increasingly perturbed, with the largest instability approaching the center of the tube, apparently in finite time.

It was noticed in [7] that the turnaround point thickness h_c computed for $a = 0.5$ cm and $L = 2\pi$ cm was very close to both the minimum film thickness required for plug formation and the minimum film thickness required for numerical solutions to exhibit unchecked growth. Here, using the traveling wave solutions computed above, this correspondence between turnaround point and plug formation is established for a variety of tube radii and period lengths. Fig. 10 shows a comparison of the critical turnaround point calculated in the previous section for six values of tube radius

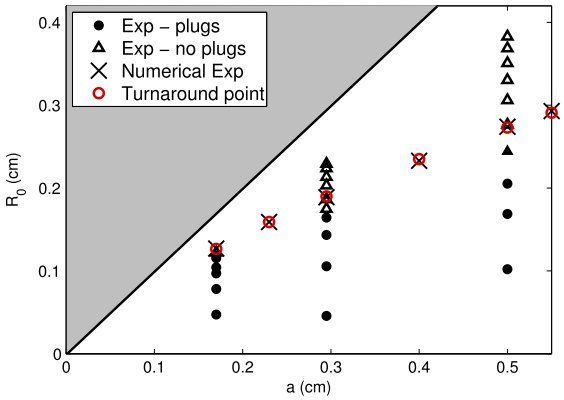

Fig. 10. Turnaround points (red open circles) for six values of h_0, and the corresponding minimum thickness which results in unchecked instability growth in (1) (black '×'s) calculated in [7]. Physical experiments from [7] which exhibited plugs (closed circles) and no plugs (open triangles) are shown as well. The closed triangle for $a = 0.5$ cm denotes an experiment which exhibited plug formation, but only intermittently. The shaded gray region denotes values of $R_0 > a$ corresponding to a film coating the exterior of the tube. (For interpretation of the references to color in this figure legend, the reader is referred to the web version of this article.)

with the corresponding experimental results and numerical experiments of [7]. For all of the radii, the three estimates of a turnaround point for critical thickness are in good agreement. We note that the small discrepancies noticeable in the graph could be due to a number of factors, both experimental and numerical, yet these differences are always within the experimental error bars. For one, since the film thickness in the physical experiments was measured with a rather crude approach making use of the weight of the fluid film and tube together (see [7]), the accuracy of the experimental measurements of the film thickness likely deteriorates with decreasing tube radius. Secondly, the numerical solutions were run for a single extended domain length (40 cm) with periodic boundary conditions and a flat interface perturbed with several small-amplitude Fourier modes; while numerical testing indicated that these results were fairly robust, this testing was not extensive.

From the comparison with experimental data, we can surmise that the model's traveling wave solutions, and their existence branch in parameter space, have a clear physical interpretation, yet to make further connection with the physics it is necessary to establish their mathematical stability. However, before tackling this issue in the next section, we conclude the current discussion by pointing out that there are other relevant qualitative differences that can further classify traveling wave solutions into two different classes. The model (1) was constructed by integrating the film's axial velocity profile across the film; the velocity field (u, w) (in the (r, z) directions where r is the radial coordinate) can then be reconstructed from the model solution and expressed succinctly in terms of the stream function

$$u = -\partial_z \Psi, \qquad w - c = \frac{1}{r}\partial_r(r\Psi), \tag{12}$$

where

$$\Psi = \left[-\frac{1}{4} + \frac{4S}{Q^2}(Q_z + Q^2 Q_{zzz})\right]\left[\frac{1}{4r}(a^2 - r^2)^2\right] + \left[\frac{Q^2}{2} - 8S(Q_z + Q^2 Q_{zzz})\right] \times \left[\frac{1}{4r}(a^2 - r^2 + 2r^2\log(r/a))\right]. \tag{13, 14}$$

Two qualitatively different types of flow within the film are possible. For relatively small-amplitude waves, the streamlines of the fluid flow are topologically equivalent to those of the flat solution; only some fanning and constricting of the streamlines mirroring the wave profile exists. For relatively high-amplitude waves, however, a region of recirculation within the wave crest can exist; this trapped core of fluid essentially rolls along the rest of the film as the wave propagates down the tube. Fig. 11 shows an example of each of these scenarios; see [32,7,10,21] for more on the existence of these trapped cores in this and related models. Interestingly, the turnaround point does not necessarily appear to correspond with a transition from waves with trapped cores to waves with no trapped cores; for most parameter combinations, this 'streamline bifurcation' occurs at a different (generally higher) point along the family of solutions.

4. Stability studies

In this section, we study stability of our computed traveling waves through a combination of linearized analysis and time dependent simulation. In related equations like Allen–Cahn, the mKdV equation, K–S or in reaction–diffusion equations, a refined stability analysis for periodic solutions have been developed in many works, see for instance [33–36,20,37–42] just to name a few. In most cases listed here, the nature of the nonlinearity allows an in depth ODE analysis to prescribe the structure of the traveling waves. In the model we are studying here, this kind of analysis is somewhat hindered by the kind of nonlinearity and its degeneracy which arises from the curved geometry of the physical setup.

In the wave reference frame $Z = z - ct$, the substitution $R(z, t) = Q(Z) + \varphi(Z, t)$ into (1) results in the following linearized evolution for φ,

$$\begin{aligned}\mu\varphi_t = &\left[\rho g f_{1z} + \frac{\gamma}{16Q}\left(g_{1z} + g_{2z} - \frac{g_{3z}}{Q}\right)\right]\varphi \\ &+ \left(\rho g f_1 + \mu c + \frac{\gamma}{16Q}(f_{2z} + g_1 + g_2)\right)\varphi_Z \\ &+ \left(\frac{\gamma}{16Q} f_2\right)\varphi_{ZZ} + \left(\frac{\gamma}{16Q} g_{4z}\right)\varphi_{ZZZ} \\ &+ \left(\frac{\gamma}{16Q} g_4\right)\varphi_{ZZZZ}.\end{aligned} \tag{15}$$

Here,

$$\begin{aligned} g_1 &= 2f_2 Q Q_{ZZZ}, \\ g_2 &= f_{2,Q}(Q_Z + Q^2 Q_{ZZZ}), \\ g_3 &= f_2(Q_Z + Q^2 Q_{ZZZ}), \\ g_4 &= f_2 Q^2, \end{aligned} \tag{16}$$

and $f_{2,Q} = \partial f_2/\partial Q = 2a^4/Q^3 - 2Q + 8Q\log(Q/a)$. With the separation of variables

$$\varphi(Z, t) = e^{\lambda t/\mu}\,\psi(Z), \tag{17}$$

the linearized evolution (15) becomes an eigenvalue problem for λ and its associated eigenfunction ψ,

$$\mathcal{L}[Q]\psi = \lambda\psi, \qquad \psi(Z + L) = \psi(Z), \tag{18}$$

with the differential operator $\mathcal{L}[Q]$ defined by the right-hand side of (15). Eigenvalues of this problem may then be found numerically, and the resulting spectrum can partially assess the linear stability of the traveling wave solution Q. A more comprehensive linear stability analysis would free the eigenfunctions ψ from satisfying periodic boundary conditions, as in principle any perturbation of the traveling wave solution Q should be permitted in a study of its stability. However, as we shall see, the restricted class of perturbations constructed from the periodic problem (18) is already sufficient to determine instability of these solutions, although in a

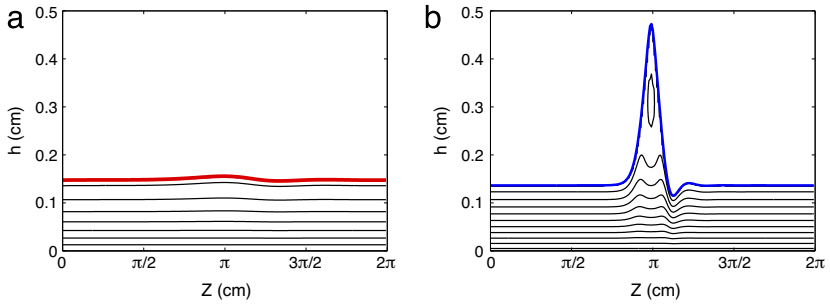

Fig. 11. (a) Lower and (b) upper branch solutions with $a = 0.5$ cm, $L = 2\pi$ cm, and $h_0 \approx 0.15$ cm. Streamlines are plotted in a frame of reference moving with the wave.

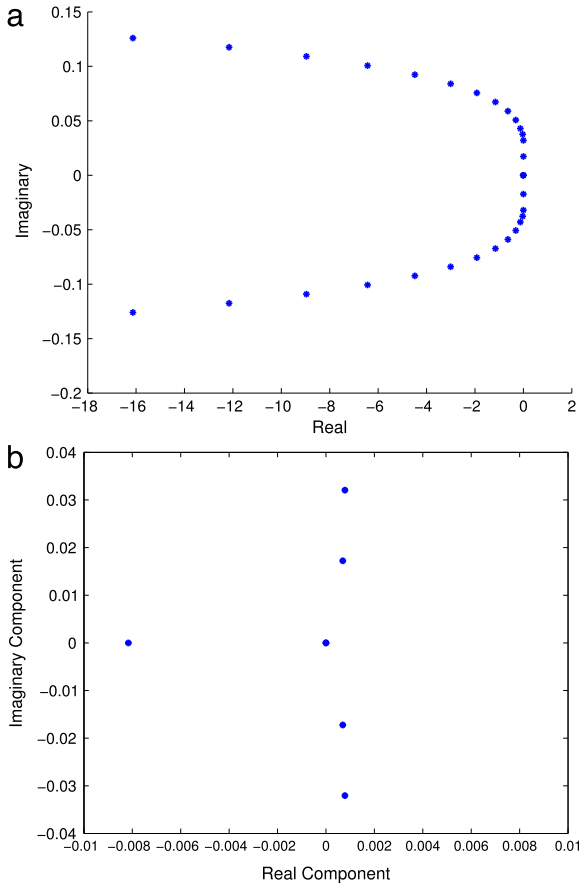

Fig. 12. (a) Linearized spectrum around the lower branch solution depicted in Fig. 4(a) for $a = 0.5$ cm, $L = 2\pi$ cm. (b) Same as (a), zooming in for a close-up of the region around the origin where eigenvalues with positive real parts are located.

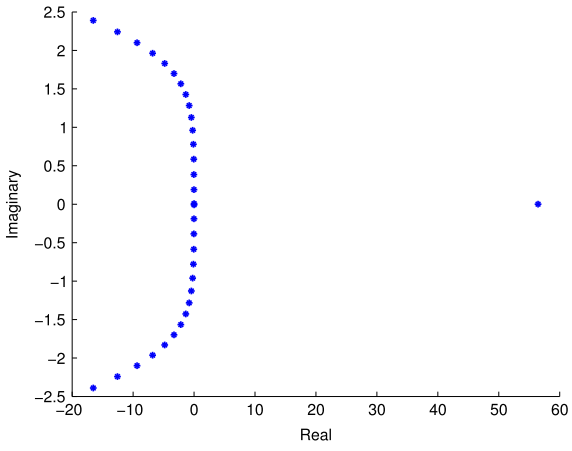

Fig. 13. Same as Fig. 12 but for the upper branch solution depicted in Fig. 4(b).

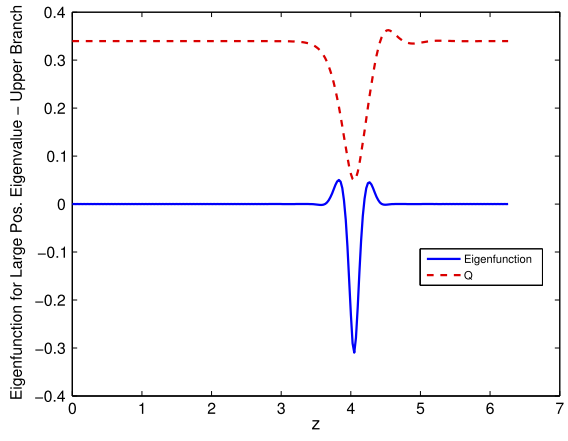

Fig. 14. The eigenfunction φ (solid line) numerically computed to correspond with the large, positive real eigenvalue for the upper branch solution Q (dashed line) in Fig. 13 with $a = 0.5$ cm. Note that $h = a - Q$ is shown in Fig. 4(b).

markedly different fashion depending on whether Q belongs to the lower or upper branch of solutions.

The spectrum of the resulting linearized operator is computed using periodic solutions from the desired part of the bifurcation curve found by *AUTO* continuation. These solutions are further refined through the Newton solver '*nsoli*' in *Matlab* to ensure they are as accurate as possible as approximations to actual solutions of (6). The resulting wave profiles are then entered in a pseudospectral implementation of the Hill's method for the linear operator in (15), and the spectrum is computed using the program '*eig*' in *Matlab*. Almost all traveling wave solutions found by our methods are linearly unstable; these solutions can be grouped into two classes: weakly unstable for waves picked along the lower branch, and strongly unstable for upper branch ones. Interestingly, the spectrum appears to have no real component eigenvalues right at the turnaround point where the two branches merge and only one traveling wave profile exists. This wave is hence neutrally stable, though of course its full stability needs to be assessed by nonlinear analysis.

The spectrum is presented for a solution from the lower branch and upper branch in Figs. 12 and 13, respectively. For the lower branch, there are two pairs of complex-conjugate eigenvalues with positive real part; the magnitude of each of these positive real components is quite small ($<10^{-4}$). In contrast, for the upper branch there is one large positive eigenvalue along with one pair of complex-conjugate eigenvalues with positive real part; each of these smaller real parts has magnitude less than 10^{-3}. The large eigenvalue corresponds to the eigenfunction shown in Fig. 14.

The transition from weakly unstable lower branch solutions to strongly unstable upper branch solutions is depicted in Fig. 15.

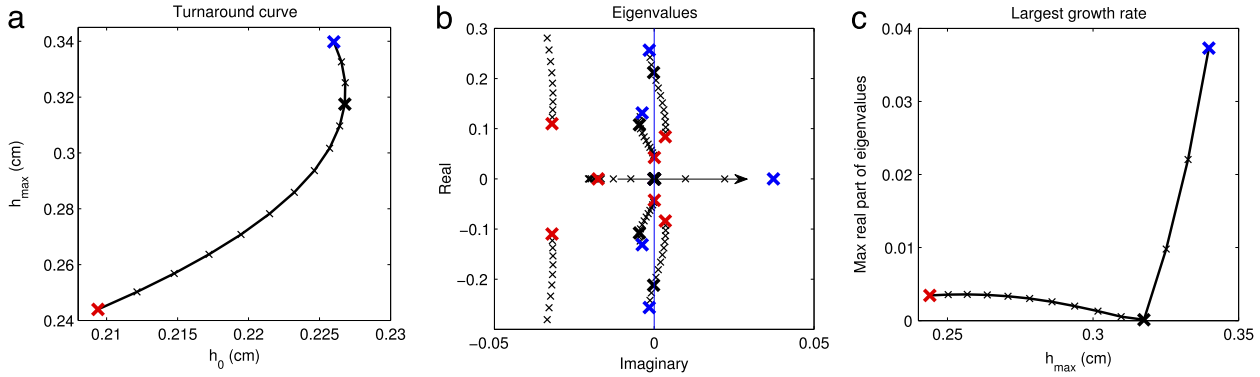

Fig. 15. (a) A portion of the turnaround curve shown in Fig. 3 for $a = 0.5$ cm. Computed solutions are denoted by an '×'. The solution with lowest (highest) $h_{\max}$ is shown with a bold red (blue) '×'; a bold black '×' is used to denote a solution close to the turnaround point. (b) Eigenvalues near the origin for each solution in panel (a). Arrow depicts the movement of one of the real eigenvalues as $h_{\max}$ increases along the turnaround curve. (c) Maximum real component of the eigenvalues for each solution in (a, b). (For interpretation of the references to color in this figure legend, the reader is referred to the web version of this article.)

The eigenvalues closest to the origin are shown for fourteen solutions near the turnaround point with $a = 0.5$ cm and $L = 2\pi$ cm in Fig. 15(b); we note that while only a few eigenvalues of the linearized operator are shown, these include the eigenvalue with largest real component for each solution. For solutions which lie on the lower branch, i.e. solutions between the bold red and black '×'s in Fig. 15(a), there is one pair of complex conjugate eigenvalues with positive real part, one zero eigenvalue, and one negative real eigenvalue, in addition to other complex conjugate pairs with negative real part; the real part of these complex eigenvalues correspond to the growth rates of the flat solution. (Note that each traveling wave solution always has a zero eigenvalue corresponding to the eigenfunction $\psi = \varphi = Q_Z$.)

Traveling up the lower branch curve towards the turnaround point, the complex conjugate pair move towards the imaginary axis, while the negative real eigenvalue moves towards the origin. As the turnaround point is passed moving further along the curve, so that the upper branch is reached, the complex conjugate pair crosses the imaginary axis while the negative real eigenvalue becomes positive; this positive eigenvalue is not a part of the flat solution's spectrum. Continuing along the upper branch, this positive real eigenvalue grows in magnitude very quickly; by $h_0 = 0.18$ cm this eigenvalue is approximately 56 (Fig. 13). The maximum of the real part of the eigenvalues for each solution is shown in Fig. 15(c); the two branches, i.e. weakly unstable lower branch solutions and strongly unstable upper branch solutions, appear to be separated by a neutrally stable traveling wave solution located at the turnaround point. For further discussion of positive eigenvalues in other gravity-driven Newtonian film flow models, including classification of instabilities as absolute or convective, see, e.g., [25,27–29]. We leave classification of these instabilities to traveling wave solutions to future work; for a discussion of instability classification for the flat solution, see [7].

In addition to corresponding to plug formation in experiments, the turnaround point distinguishes between these two types of unstable traveling waves. We note that the solution denoted by the bold black '×' appears to be the best approximation of the location of this transition in panels (b) and (c), while it appears to lie slightly below the turnaround point in panel (a). This small apparent discrepancy is due to having displayed the turnaround curve as a function of mean film thickness h_0; when the curve is displayed as a function of volume, i.e. R_0^2 (not shown), this solution marked by the bold black '×' is a very good approximation of the turnaround point.

The stability results are also illustrated with time-dependent direct numerical simulations of (1), using a pseudospectral code carefully designed to eliminate the effects of aliasing in this nonlinear equation; see [43,7] for more details. The traveling wave solutions with period $L = 2\pi$ cm are used as initial conditions; these initial conditions are not perturbed other than by the presence of numerical error accumulated during their computation. The time evolution of solutions to (1) is dominated by a combination of traveling wave pulses and the stability properties of the flat solution. As shown by the dispersion relation (4), given a film thickness $a - R_0$ and fixed physical parameters ρ, etc., for sufficiently short periods $L < 2\pi\sqrt{2}R_0$ the flat solution is stable with respect to periodic perturbations of period L. As L increases, discrete wave numbers $k_n = 2\pi n/L$ enter the window of instability $0 < k < R_0^{-1}$, with $n = 1, \ldots [L/R_0]$ ($[\cdot]$ denotes integer part). The ensuing increase in unstable degrees of freedom as L increases makes for increasingly complex dynamics as small perturbations of the flat solutions evolve and saturate the nonlinear terms governing the evolution. This saturation eventually assumes the form of a sequence of pulses, which in profile appear in Figs. 16 and 17 for periods 2π and 8π respectively.

This behavior qualitatively resembles that of other models studied in the literature. In fact, the thin-film, flat-geometry limit of this model can be reduced to the well-known K–S equation, see [44,45,21], and the dispersion relation (4) exactly coincides with that of the K–S equation. Thus, when saturation of the instability occurs at low-amplitude waves, i.e., the nonlinearity is weak, the dynamics can be expected to closely resemble that of the K–S equation, including its chaotic main features. In contrast, the evolution of larger amplitude waves is more reminiscent of the dynamics seen in the so-called St. Venant roll waves studied in [20,37]. There the authors observe that the flat component of the wave can lead to instability in the form of very small eigenvalues with positive real part, though in such a case the authors argue that the stability of the non-flat part of the pulse tends to damp these instabilities when the pulses are spaced sufficiently close together; Fig. 18 shows the evolution of a traveling wave solution for $L = 8\pi$ cm with larger amplitude than that shown in Fig. 17.

In Fig. 19, the evolution of an upper branch solution is shown, where the solution with $a = 0.5$ cm, $L = 2\pi$ cm, and $h_0 \approx 0.2$ cm has been used as an initial condition in the solver for (1). Rapid decay in the amplitude of the wave is seen, so that by $t = 90$ s the upper branch solution has approached a profile close to that of a lower branch solution; for comparison, an actual lower branch solution with similar mean thickness is included in the plots. Consistent with the discussion above, however, this smaller-amplitude wave continues to evolve with the nearly-flat region developing visible instability by $t = 300$ s.

5. Conclusions

This study of traveling wave solutions of a gravity-driven film-flow model expands on the findings of [7] of a 'saddle–node'-type bifurcation of different branches of traveling wave solutions,

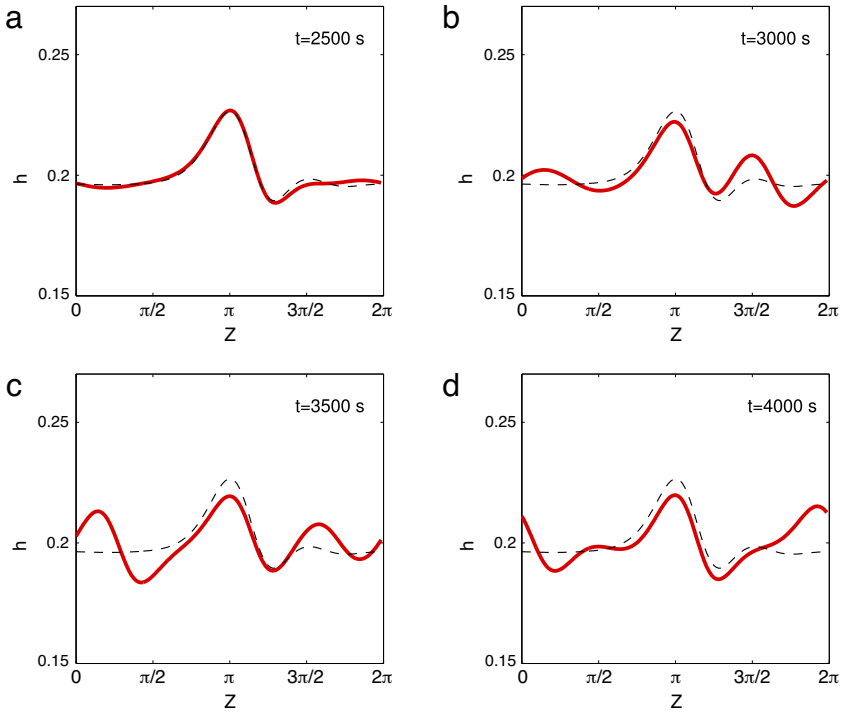

Fig. 16. Snapshots of the evolution of a lower branch traveling wave solution with $a = 0.5$ cm, $L = 2\pi$ cm, $h \approx 0.202$ cm at (a) $t = 2500$ s, (b) $t = 3000$ s, (c) $t = 3500$ s, and (d) $t = 4000$ s. The original traveling wave solution used as the initial condition is shown by the dashed black line. Solutions have been shifted so that the maximum h is located in the center of the domain for all snapshots.

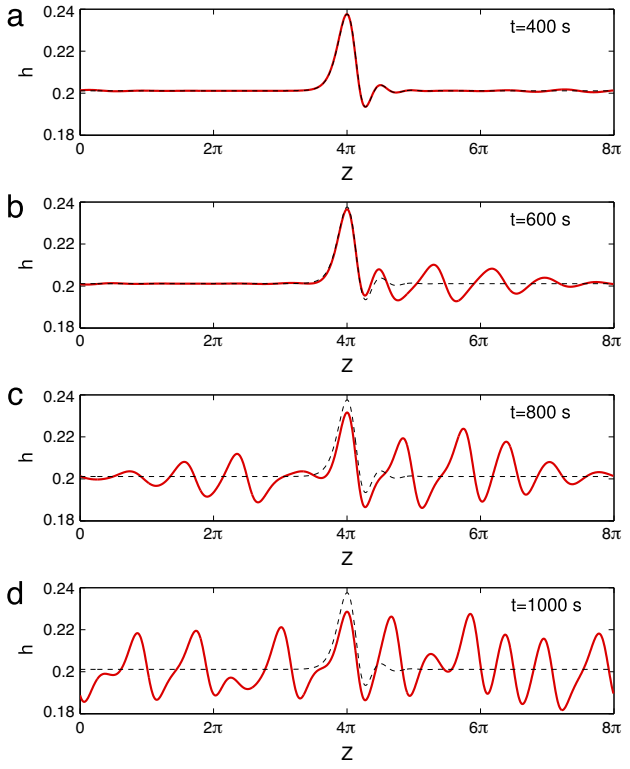

Fig. 17. Same as Fig. 16 but for $L = 8\pi$ cm; snapshots are shown for (a) $t = 400$ s, (b) $t = 600$ s, (c) $t = 800$ s, and (d) $t = 1000$ s.

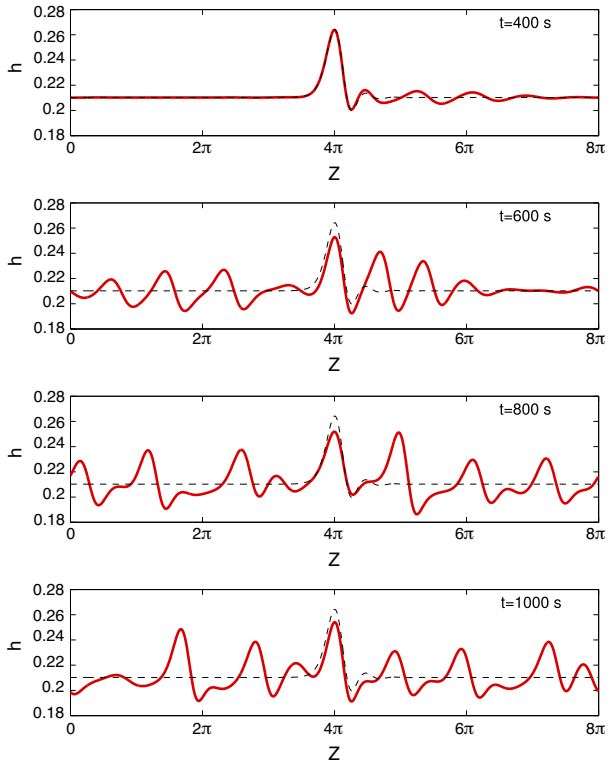

Fig. 18. Same as Fig. 17 but for $h_0 = 0.213$ cm; snapshots are shown for (a) $t = 400$ s, (b) $t = 600$ s, (c) $t = 800$ s, and (d) $t = 1000$ s.

and provides additional evidence for the physical relevance of the 'turnaround point' along each solution branch. This turnaround point identifies a traveling wave solution of maximum film thickness for a given branch, and this critical thickness appears to be a reasonably accurate tool to predict the onset of plug formation in actual experiments over a fairly wide range of parameter values. This agreement is remarkable considering both the different boundary conditions specified in the model and the

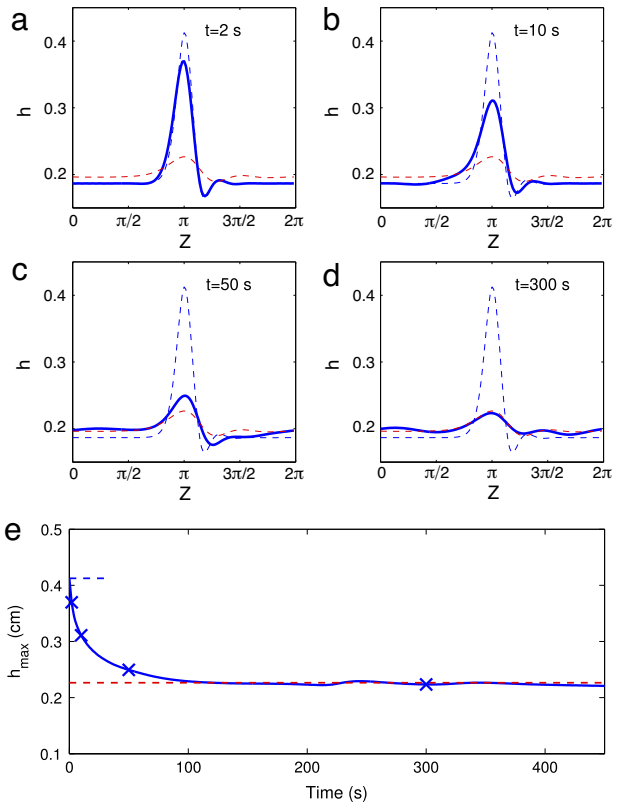

Fig. 19. (a)–(d) Snapshots from the evolution of the upper branch solution with $h_0 \approx 0.2$ cm, $a = 0.5$ cm, and $L = 2\pi$ cm at (a) $t = 2$ s, (b) $t = 10$ s, (c) $t = 50$ s, (d) $t = 300$ s, with the wave shifted so that the crest is located at $z = \pi$ cm. The initial condition (dashed blue line) and corresponding lower branch solution (dashed red line) are also shown. (e) Maximum value of $h(z, t)$ for the evolution of the upper branch solution for each time $t < 450$ s. Blue $\times$'s correspond to panels (a)–(d). Dashed lines show $h_{\max}$ for the upper branch solution (blue) and the corresponding lower branch solution (red). (For interpretation of the references to color in this figure legend, the reader is referred to the web version of this article.)

experiments, and the simplifying asymptotic assumptions made in deriving the model.

The study of the stability of these solutions using Hill's method shows that all the solutions discussed here are linearly unstable. The nature of the instability, however, is qualitatively and quantitatively different for solutions on an upper branch (large amplitude) than those on a lower branch (small amplitude). While the linearized operator for solutions along either branch may contain some eigenvalues with small positive real component (likely reflecting the instability of the nearly flat region of the solution away from the wave crest), in all cases we have analyzed of upper branch solutions the spectrum of this operator also contains one large real eigenvalue. Numerical simulations of the evolution of these large-amplitude waves show early rapid decay to a close approximation of the corresponding lower branch solution, followed by the slow instability growth, corresponding to the flat region of the film, similar to that of the lower branch solution of equal mean thickness. For low amplitude mean thicknesses, and hence small amplitude traveling waves, the dynamics of these solutions and the number of unstable modes corresponding to each solution is reminiscent of studies of the K–S equation. In addition, evolution of sufficiently long flat solutions whose mean is lower than the maximum amplitude set by the turnaround point results in a train of pulses resembling those from the lower branch, with amplitudes and pulse widths essentially determined by mean thickness and period length. An analytic understanding of the qualitative differences in the evolution of films governed by our model would likely highlight the stabilizing effects of the dispersive terms in the governing equation, similarly to the role played by the KdV component in the studies carried out in [20].

Given its relevance, an analytical expression for the turnaround point location depending on the model parameters would clearly be desirable. A possible approach to obtain such a formula could be offered by focusing on the solitary wave solutions, which, while not proven to exist for our model, are made plausible by our continuation of traveling wave solution for increasing periods. Solitary waves are essentially the tool exploited by the analysis of [18], thanks to the analytical tools available to determine homoclinic orbits in dynamical systems of Sil'nikov type. This is a possible interpretation of the third order ODE system that determines traveling wave solutions for our model and other related thin-film equations. However, important differences exist between the interior problem we have studied and that of the film coating the exterior of a cylinder of [18]. Non-existence of solitary waves in that case had been related to finite time blow-up of solutions, which in turn was taken as the model's way of predicting droplet formation. We notice that the thin-film model used in [18] is in all likelihood preventing the bifurcation structure with upper and lower branch we have observed, besides the fact that our interior problem offers the natural upper bound of the cylinder's radius to the amplitude growth of waves, in contrast to the unchecked growth possible for the exterior problem. In fact, it would be interesting to extend the present study to the counterpart of our model for the exterior problem, developed in [6]. This could provide further insight on the physical significance of the branched structure of traveling wave solutions. For instance, it would be desirable to understand the dynamical origin of this structure, which could be due to the underlying cylindrical geometry of the setup. For example, if two-solution branches exist for both interior and exterior problems, they could represent a balance of surface tension forces due to the two different curvatures at play (longitudinal versus radial), and this might occur at different amplitudes given the different curvatures at the peaks of small versus large waves.

Further study is also needed for expanding the physical setups and parameters, such as modeling non-trivial air flow in the tube, non-perfect cylindrical tubes, inclined tubes, etc., as well as to further assess the role of traveling waves in actual fluid transport. However, the tools developed here give a very simple computational dynamics approach to prediction in the experiments of [7]. As a result, this study gives some insights into the role traveling waves play in the physics of viscous fluid flow in cylindrical geometries and develops tools that will be required to address more complex physical questions in related problems.

Acknowledgments

This work is motivated by the Virtual Lung Project at UNC. RC and RO were partially supported by National Science Foundation grants DMS-0908423, DMS-1009750, RTG DMS-0943851, and by NIEHS 534197-3411. JM and NV were supported in part by National Science Foundation grants DMS-1312874 and CAREER DMS-1352353. Additional partial support for NV by National Science Foundation grants DMS-0800678 and DMS-1054289 is also acknowledged. RC thanks the Bernoulli Center of EPFL and the Department of Mathematics and Application of UNIMIB for their hospitality while parts of this work were carried out. JM wishes to thank the Hausdorff Institute for Mathematics and the Schrödinger Institute for hosting him during the completion of parts of this work. We are very grateful to Gideon Simpson for assistance setting up simulations of thin film equations in AUTO. Discussions with Mat Johnson and Olga Trichtchenko are gratefully acknowledged.

Appendix. Model in dimensionless form

The dimensionless form of the model equation (1) is given by:

$$R_t = f_1(R;a)R_z + \frac{\epsilon}{16\,Bo\,R}[f_2(R;a)(R_z + \epsilon^2 R^2 R_{zzz})]_z, \tag{A.1}$$

where $Bo = \rho g h_0^2/\gamma$ is the Bond number, and where $\epsilon = h_0/\lambda_0$ is an aspect ratio. The scales used to nondimensionalize (1) are

$$R^* = R/h_0, \qquad z^* = z/\lambda_0, \qquad t^* = tW_0/\lambda_0, \tag{A.2}$$

where $h_0 = a - R_0$ is the mean thickness of the fluid film, λ_0 is a typical wavelength of a free-surface disturbance, and $W_0 = \rho g h_0^2/\mu$ is the velocity scale, and where stars have been dropped in (A.1).

Likewise, the dimensionless conservation law form of the model is

$$8(R^2)_t = \left\{ f_2(R;a)\left[-R^2 + \frac{\epsilon}{B_o}(R_z + \epsilon^2 R^2 R_{zzz}) \right] \right\}_z . \tag{A.3}$$

References

[1] D.J. Benney, Long waves in liquid films, J. Math. Phys. 45 (1966) 150–155.
[2] S.P. Lin, Finite amplitude side-band stability of a viscous film, J. Fluid Mech. 63 (1974) 417–429.
[3] A.L. Frenkel, Nonlinear theory of strongly undulating thin films flowing down vertical cylinders, Europhys. Lett. 18 (1992) 583–588.
[4] S.P. Lin, W.C. Liu, Instability of film coating of wires and tubes, AIChE J. 24 (1975) 775–782.
[5] I.L. Kliakhandler, S.H. Davis, S.G. Bankoff, Viscous beads on vertical fibre, J. Fluid Mech. 429 (2001) 381–390.
[6] R.V. Craster, O.K. Matar, On viscous beads flowing down a vertical fibre, J. Fluid Mech. 553 (2006) 85–105.
[7] R. Camassa, H.R. Ogrosky, J. Olander, Viscous film flow coating the interior of a vertical tube. Part I. Gravity-driven flow, J. Fluid Mech. 745 (2014) 682–715.
[8] R.V. Craster, O.K. Matar, Dynamics and stability of thin liquid films, Rev. Modern Phys. 81 (2009) 1131–1198.
[9] R.V. Roy, A.J. Roberts, M.E. Simpson, A lubrication model of coating flows over a curved substrate in space, J. Fluid Mech. 454 (2002) 235–261.
[10] R. Camassa, H.R. Ogrosky, On viscous film flows coating the interior of a tube: thin-film and long-wave models, J. Fluid Mech. 290 (2015) 131–166.
[11] S.L. Goren, The instability of an annular thread of fluid, J. Fluid Mech. 27 (1962) 309–319.
[12] C.-S. Yih, Instability due to viscosity stratification, J. Fluid Mech. 27 (1967) 337–352.
[13] C. Hickox, Instability due to viscosity and density stratification in axisymmetric pipe flow, Phys. Fluids 14 (1971) 251–262.
[14] G.I. Sivashinsky, D.M. Michelson, On irregular wavy flow of a liquid down a vertical plane, Progr. Theoret. Phys. 63 (1980) 2112–2114.
[15] A. Pumir, P. Manneville, Y. Pomeau, On solitary waves running down an inclined plane, J. Fluid Mech. 135 (1983) 27–50.
[16] C. Ruyer-Quil, P. Manneville, Improved modeling of flows down inclined planes, Eur. Phys. J. B 6 (1998) 277–292.
[17] V.I. Kerchman, A.L. Frenkel, Interactions of coherent structures in a film flow: Simulations of a highly nonlinear evolution equation, Theor. Comput. Fluid Dyn. 6 (1994) 235–254.
[18] S. Kalliadasis, H.-C. Chang, Drop formation during coating of vertical fibers, J. Fluid Mech. 261 (1994) 135–168.
[19] E. Doedel, B. Oldeman, et al. AUTO-07P, Software Package and User Manual.
[20] M.A. Johnson, P. Noble, L.M. Rodrigues, K. Zumbrun, Spectral stability of periodic wave trains of the Korteweg–de Vries/Kuramoto–Sivashinsky equation in the Korteweg–de Vries limit, Trans. Amer. Math. Soc. 367 (3) (2015) 2159–2212.
[21] V. Kerchman, Strongly nonlinear interfacial dynamics in core-annular flows, J. Fluid Mech. 772 (1995) 569–599.
[22] Y. Cho, Computation of steady gravity–capillary waves on deep water based on the pseudo-arclength continuation method, Comput. & Fluids 96 (13) (2014) 253–263.
[23] Z. Wang, J.-M. Vanden-Broeck, P.A. Milewski, Asymmetric gravity–capillary solitary waves on deep water, J. Fluid Mech. 759 (2014) R2.
[24] N.J. Balmforth, G.R. Ierley, E.A. Spiegel, Chaotic pulse trains, SIAM J. Appl. Math. 54 (1994) 1291–1334.
[25] C. Duprat, F. Giorgiutti-Dauphiné, D. Tseluiko, S. Saprykin, S. Kalliadasis, Liquid film coating a fiber as a model system for the formation of bound states in active dispersive-dissipative nonlinear media, Phys. Rev. Lett. 103 (2009) 234501-1–234501-4.
[26] C. Elphick, G.R. Ierley, O. Regev, E.A. Spiegel, Interacting localized structures with Galilean invariance, Phys. Rev. A 44 (1991) 1110–1122.
[27] M. Pradas, D. Tseluiko, S. Kalliadasis, Rigorous coherent-structure theory for falling liquid films: viscous dispersion effects on bound-state formation and self-organization, Phys. Fluids 23 (2011) 044104-1–044104-19.
[28] D. Tseluiko, S. Saprykin, C. Duprat, F. Giorgiutti-Dauphiné, S. Kalliadasis, Pulse dynamics in low-Reynolds-number interfacial hydrodynamics: Experiments and theory, Physica D 239 (2010) 2000–2010.
[29] D. Tseluiko, S. Kalliadasis, Weak interaction of solitary pulses in active dispersive-dissipative nonlinear media, IMA J. Appl. Math. 79 (2014) 274–299.
[30] C. Ruyer-Quil, S. Kalliadasis, Wavy regimes of film flow down a fiber, Phys. Rev. E 85 (2012) 046302-1–046302-23.
[31] C. Ruyer-Quil, P. Treveleyan, F. Giorgiutti-Dauphiné, C. Duprat, S. Kalliadasis, Modelling film flows down a fibre, J. Fluid Mech. 603 (2008) 431–462.
[32] R. Camassa, M.G. Forest, L. Lee, H.R. Ogrosky, J. Olander, Ring waves as a mass transport mechanism in air-driven core-annular flows, Phys. Rev. E 86 (2012) 066305-1-11.
[33] B. Deconinck, M. Nivala, The stability analysis of the periodic traveling wave solutions of the mKdV equation, Stud. Appl. Math. 126 (2011) 17–48.
[34] B. Nicolaenko, B. Scheurer, R. Temam, Some global dynamical properties of the Kuramoto–Sivashinsky equations: nonlinear stability and attractors, Physica D 16 (1985) 155–183.
[35] B. Sandstede, A. Scheel, Absolute and convective instabilities of waves on unbounded and large bounded domains, Physica D 145 (2000) 233–277.
[36] J. Bronski, M. Johnson, T. Kapitula, An index theorem for the stability of periodic travelling waves of Korteweg–de Vries type, Proc. Roy. Soc. Edinburgh Sect. A 141 (2011) 1141–1173.
[37] B. Barker, M.A. Johnson, P. Noble, L.M. Rodrigues, K. Zumbrun, Stability of viscous St. Venant roll-waves: from onset to the infinite-Froude number limit, Pre-Print (2015). arXiv:1503.01154.
[38] D. Ginsberg, G. Simpson, Analytical and numerical results on the positivity of steady state solutions of a thin film equation, Discrete Contin. Dyn. Syst. Ser. B 18 (5) (2013) 1305–1321.
[39] C.W. Curtis, B. Deconinck, On the convergence of Hill's method, Math. Comp. 79 (2010) 169–187.
[40] B. Deconinck, J.N. Kutz, Computing spectra of linear operators using the Floquet–Fourier–Hill method, J. Comput. Phys. 219 (2006) 296–321.
[41] R.S. Laugesen, M.C. Pugh, Energy levels of steady states for thin-film-type equations, J. Differential Equations 182 (2) (2002) 377–415.
[42] R.S. Laugesen, M.C. Pugh, Linear stability of steady states for thin film and Cahn–Hilliard type equations, Arch. Rat. Mech. Analysis. 154 (1) (2000) 3–51.
[43] H.R. Ogrosky, Modeling liquid film flow inside a vertical tube (Ph.D. Thesis), University of North Carolina, 2013.
[44] J.M. Hyman, B. Nicolaenko, The Kuramoto–Sivashinsky equation: A bridge between PDE's and dynamical systems, Physica D 18 (1986) 113–126.
[45] J.M. Hyman, B. Nicolaenko, S. Zaleski, Order and complexity in the Kuramoto–Sivashinsky model of weakly turbulent interfaces, Physica D 23 (1986) 265–292.